Event-based imaging velocimetry applied to a cylinder wake flow in air

C. Willert[1,*], J. Klinner[1]

1: Institute of Propulsion Technology, German Aerospace Center (DLR), Köln, Germany
*Corresponding author: chris.willert@dlr.de

Keywords: fluid flow measurement, particle imaging, event-based vision sensing, dynamic vision sensor, neuromorphic imaging, high-speed imaging, time-resolved PIV, particle tracking, PTV, proper orthogonal decomposition, SPOD

ABSTRACT

Event-based vision is a new upcoming field within the field of computer vision. Unlike conventional frame-based imaging, event-based vision (or dynamic vision sensing) asynchronously records binary signals of contrast changes at the pixel level with microsecond resolution. Event-based imaging of small particles illuminated by a laser or other continuous light source generates streaks of events in a space-time domain. From this data the particles' position in both space and time can be inferred. The present work explores the possibilities of harnessing the potentials of event-based vision for fluid flow measurement with focus on two-dimensional, two-component velocity field estimation at particle image densities corresponding to that of conventional PIV. Three different motion detection schemes are implemented. Measurements of a cylinder wake flow demonstrate that EBIV provides time resolved velocity data that is suitable for the retrieval of flow statistics as well as spectral and modal analysis. The present work is an extension of the recently published Exp. Fluids article by the authors on event-based imaging velocimetry (Willert & Klinner, 2022) and provides further details on current limitations related to event-based imaging.

1. Introduction

Event-based vision (EBV), also referred to as dynamic vision sensing (DVS) or neuromorphic imaging, constitutes a new approach to motion-related imaging. Unlike conventional frame-based image sensors, an EBV sensor only records intensity changes, that is, contrast change events, on the pixel level. As each pixel operates on its own, the resulting event data stream is asynchronous in nature, varying from quiescent in static imagery and increasing to considerable data rates for scenes with high dynamic content. Consequently, the associated event-data processing requires a partial departure from the established concepts of frame-based image processing.

The underlying concepts were originally proposed by Mahowald (1992) in the early 1990's and were aimed at mimicking the functionality of the eye's retina - hence coining the name "silicon retina" in her work. By the late 2000's the technology had matured enough to result in useable

prototype cameras based on event-based sensors with pixel area on the order of 128×128 elements (Lichtsteiner et al., 2008). More recently, several companies have introduced fully integrated commercial grade event-cameras with detector arrays up to 1 MPixel (Finateu et al., 2020). This improved accessibility to event cameras has greatly expanded the areas of event-based vision applications and has made the present study possible. Comprehensive overviews of the current status of event-based vision, its range applications and associated data processing are provided by Gallego et al. (2022) and Tayarani-Najaran & Schmuker (2021). Beyond this, a Github repository maintained by the Robotics and Perception Group (2022) of the University of Zurich provides an extensive collection of literature and resources on the subject.

In the following, the working principles of event-based imaging are briefly outlined before describing its application in the context of particle imaging. The material presented herein extends on a recent paper by the authors (Willert & Klinner, 2022) and is intended to supplement the previous publication.

2. Event sensor operation and signal processing

Each EBV pixel consists of a photodiode with adjoining contrast change detection unit and logical unit (Fig. 1). Photons collected by the photodiode induce a photocurrent that is converted to a voltage. The logarithm of this voltage is supplied to the contrast detection unit allowing it to trigger change events at a fixed relative contrast threshold, typically on the order of 10-25%. A discriminator distinguishes between positive and negative intensity change events, where *positive* refers to an intensity change from dark to bright and *negative* from a brighter to a dark intensity. Once a pixel detects a positive or negative event the logical units sends out an acknowledge request to the detector's event monitors which then register the event and transmits the event's time-stamp t_i, its polarity p_i and pixel coordinates (x_i, y_i) to the output data stream. Once a pending event has been acknowledged, the logical unit resets the detector part of the pixel allowing a further event to be captured.

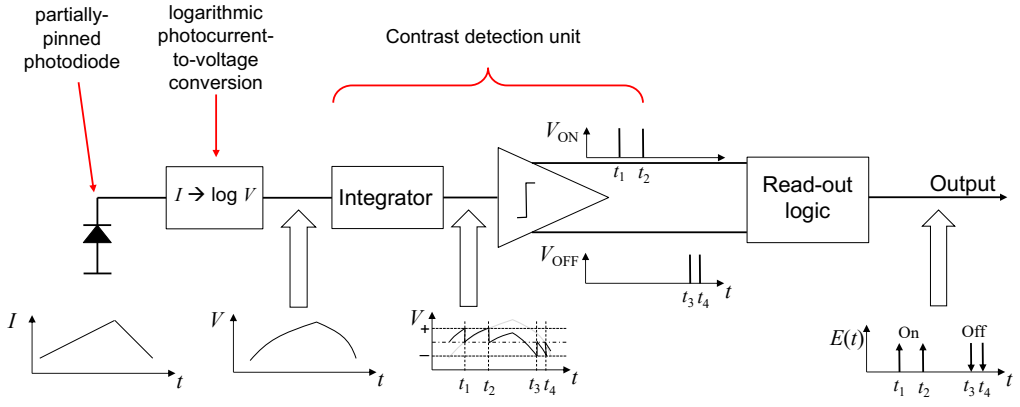

Figure 1. Simplified schematic of an EBV pixel and associated signals at each step.

2.1. Visualization of EBV data

The visualization of the recorded spatio-temporal events typically relies on so-called *pseudo-images* that are compiled from the events within a given time-interval or *time-slice*. Positive and negative events can be distinguished by rendering them with different colors as shown in Fig. 2a. Color-coding the event times results in pseudo-images containing *event-surfaces* or *time-surfaces* (c.f. Fig. 2b). These time-surface have a characteristic slope when viewed in a space-time projection such as shown in top right sub-figure of Fig. 2. The slope is directly related to the speed of the imaged object and is the quantity of interest for event-based particle imaging velocimetry.

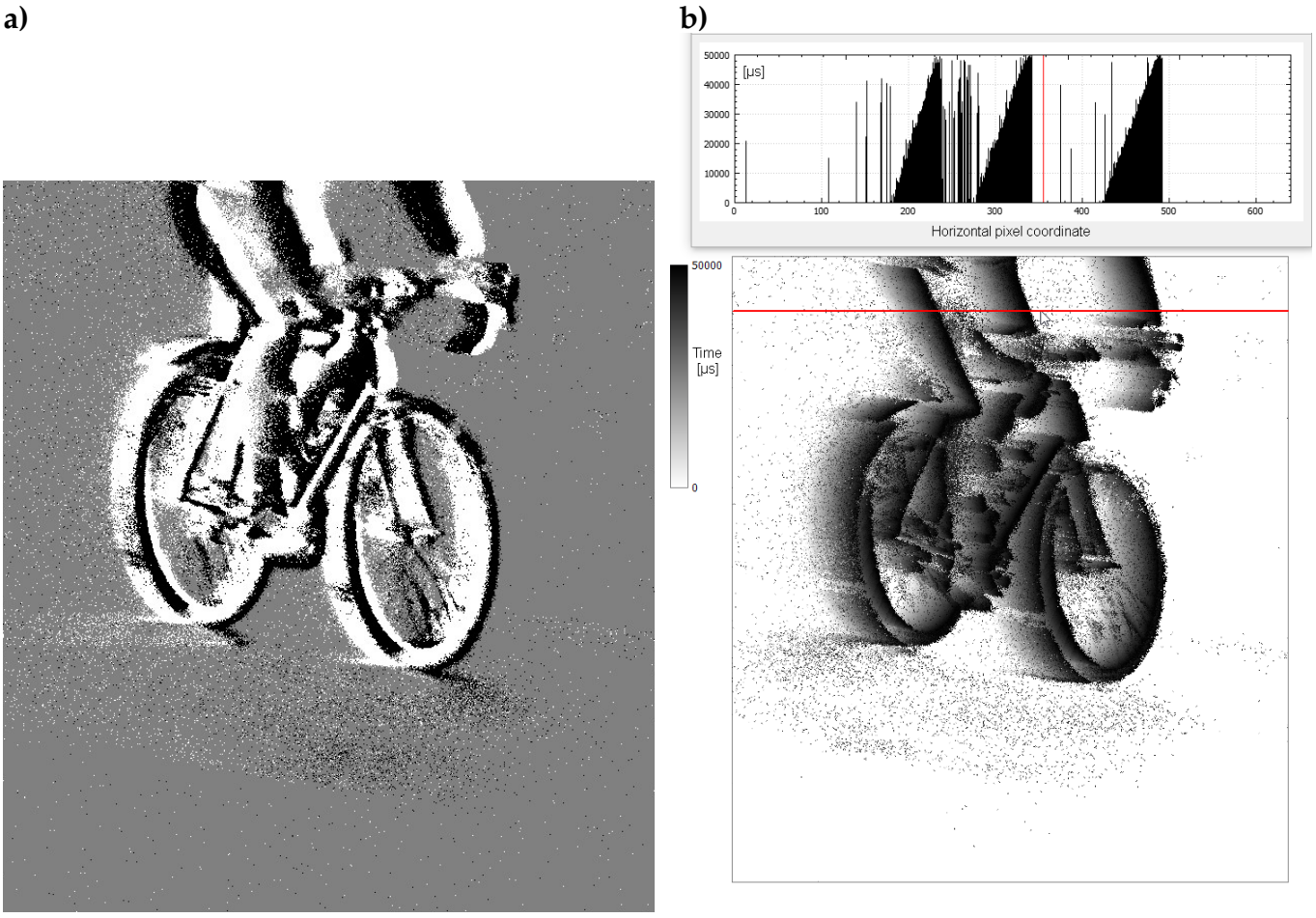

Figure 2. Pseudo-images generated from a 20 ms time-slice of events obtained by imaging a passing bicyclist; **a:** positive events are in white, negative events in black color. **b:** pseudo-image of *time-surfaces* containing 50 ms of positive events gray-coded by the relative event time t_i. The upper sub-figure shows the intensity profile along a horizontal row of pixels as indicated by the red line.

2.2. Limitations of EBV sensors

With increasing number of events per unit time, the event monitors, termed *arbiters*, reach their maximum throughput capacity and can no longer react promptly to pending event requests. This

results in a latency between the time assigned to the event and the actual occurrence of the event, and may sometimes differ by up to several hundred µs. The event overload may manifest itself differently, depends on the sensor architecture and is one of the primary challenges in low-latency event-sensor design.

For the presently used hardware, the arbiter overload results in horizontal stripes of events all of which are assigned with the same event time (see Fig. 3). The effect can be monitored with histograms of the event times. The event rate can be fine tuned not to result in arbiter overloading by changing the light intensity – here, laser power and lens aperture – or particle seeding density and was found to be in the range of 50 ev/(pixel · s) for the HD sensor (1280 × 720 pixels). Alternatively, a reduction of the field of view can be applied to increase the event-count per pixel as the arbiters can process a reduced number of pixels more efficiently .

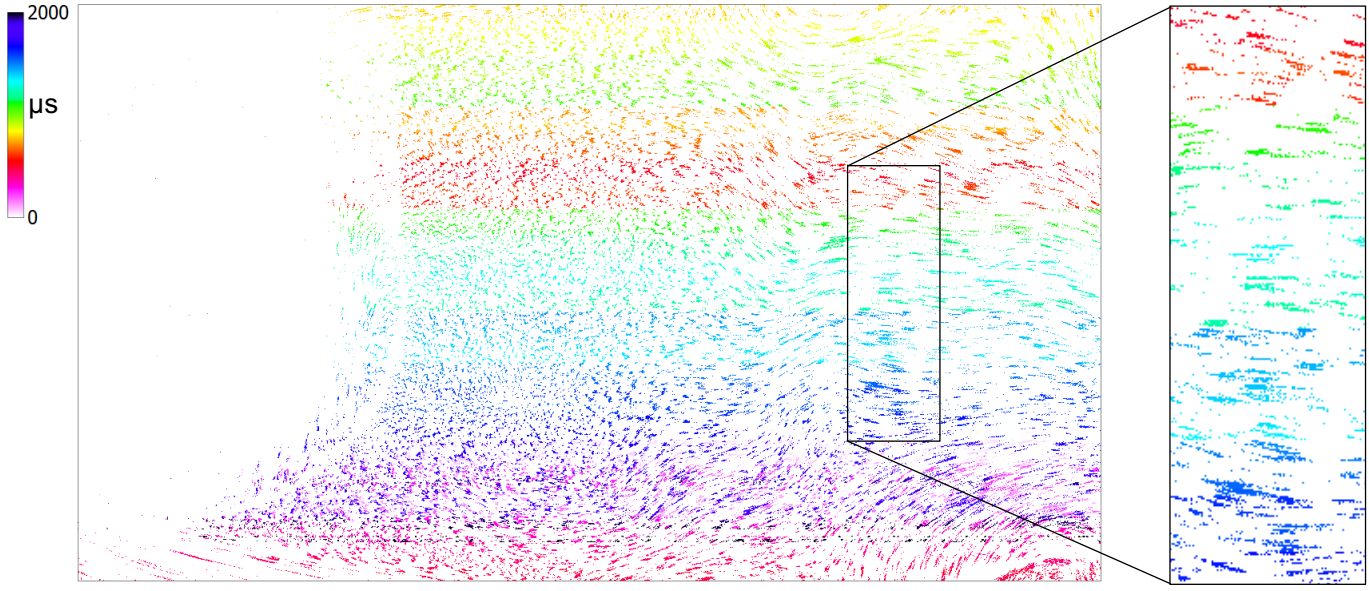

Figure 3. Example of the loss of event-timing due overload of event-monitoring units (arbiters) within the sensor itself. The pseudo-image contains 2 ms of events acquired in the wake of a circular cylinder.

3. EBIV of a cylinder wake

The initial cylinder wake flow experiments reported by Willert & Klinner (2022) demonstrated the limitations of the current EBV technology in the context of fluid flow measurements. Specifically it was found that the responsivity of an event pixel depends on the speed with which the particle image traverses the sensor's pixels. Assuming constant brightness, faster moving particle images result in a reduced number of photons being collected per unit time by the photodiode such that the likelihood of generating an event reduces with increasing particle speed. This effect can be observed in the outer flow area of Fig. 5a. In this particular imaging configuration (5W laser, 1 µm particles, high image magnification) reliable velocity measurements could be achieved up to ≈1.5 m/s corresponding to about 30 000 pixel/s on the detector.

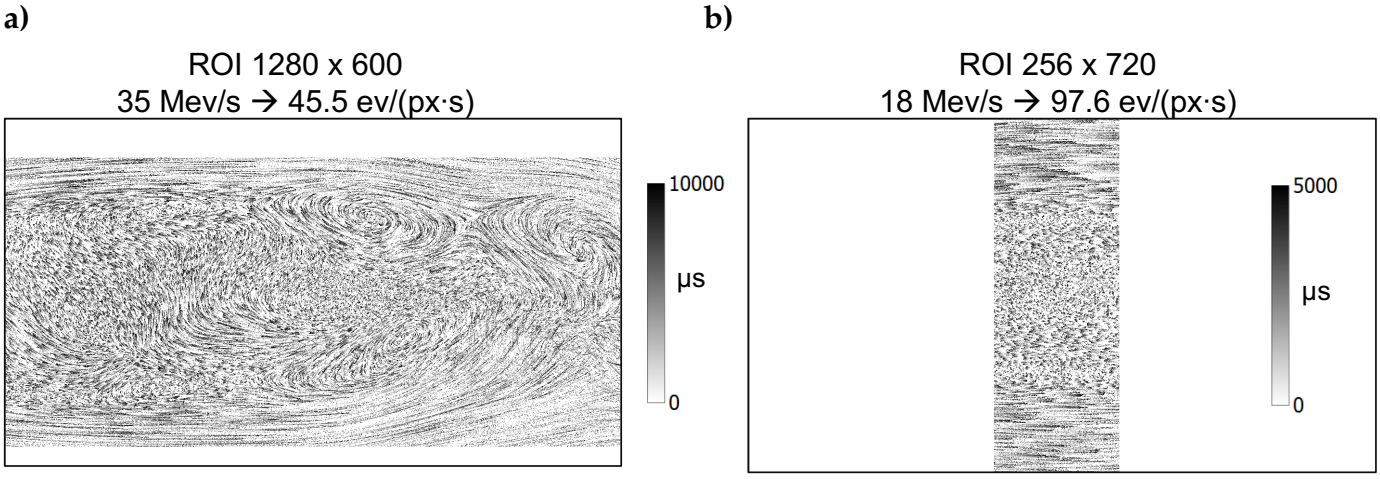

Figure 4. Reduction of the number of active event pixels allows to locally increase the event-count per pixel, **a:** ROI reduction in the vertical direction, **b:** reduction to a narrow vertical strip.

Within the context of the present work, additional wake flow experiments were performed with the intention of improving overall data quality. By limiting the region of interest (ROI), the event data rate in the area of interest could be increased. A further data rate increase was achieved by"detuning" the detector to only record positive events as only these are currently being used in the velocity field estimation. Finally the bulk flow velocity was reduced from ≈1.5 m/s to about ≈0.8 m/s. Fig. 5b shows increased data rates along with an overall more uniform event data rate distribution. This approach was used to perform measurements of the cylinder wake flow described in the following.

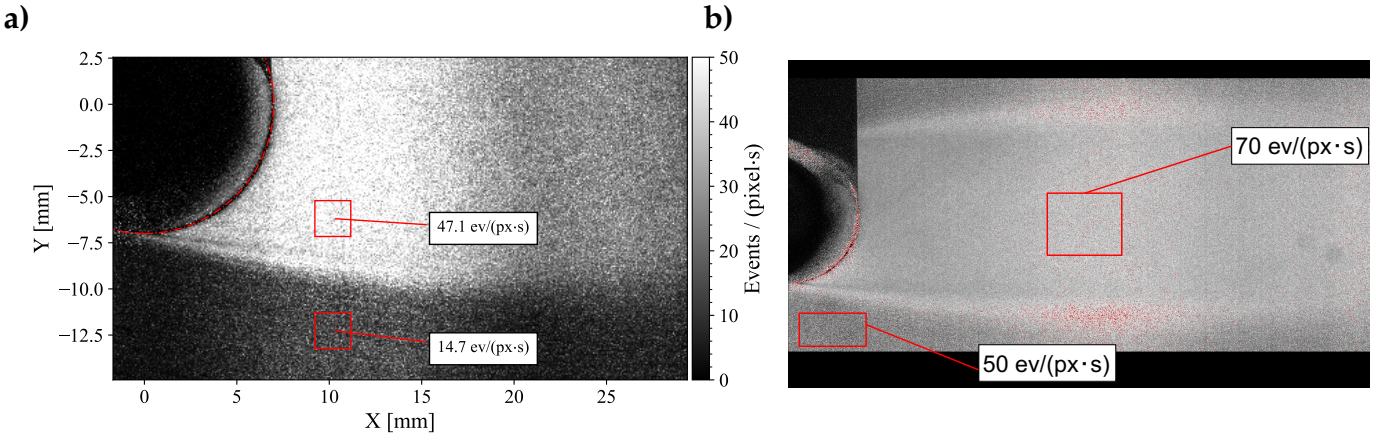

Figure 5. Event frequencies in the near wake of a cylinder, before (**a**) and after (**b**) adjustment of the event detection thresholds to record positive events only.

EBIV measurements were performed downstream of a $d = 10\,\mathrm{mm}$ cylinder with a corresponding Reynolds number of $\mathrm{Re}_D \approx 530$ which is in a range of producing a fully turbulent vortex street. The cylinder was placed on the centerline of a small wind tunnel of $76 \times 76\,\mathrm{mm}^2$ cross-section. A laser light sheet of 1 mm thickness and about 150 mm width was provided by a 5.6 W CW laser (Kvant Laser, λ = 520 nm) and illuminated the cylinder from the side. The event camera (Prophe-

see EVK-HD2, 1280×720 pixels) was fitted with a 55 mm lens (Nikon Micro-Nikkor 55/2.8) with the aperture varied between f/4.0 and f/5.6. The detection thresholds (biases) of the event camera were tuned to favor positive events as described in the previous section. With the field of view set at 43 × 20 mm^2 (M = 0.143) several event sequences were recorded at different positions downstream of the cylinder. Event rates of ≈50 Mev/s (135 MB/s) could be realized without noticeable arbiter overflow. Sequences of up to 10 s duration were acquired. For a vortex shedding frequency of about 20 Hz roughly 200 cycles were captured.

3.1. EBIV processing and results

Conventional cross-correlation PIV processing was used to extract time-resolved velocity field data from the event recordings. The necessary frame-based image data was provided in form of pseudo-images assembled from event time-slices of 400 µs duration using only positive events (dark-to-bright contrast changes). The event time-stamps were not used and all active pixels were set to the same intensity. Triple-frame correlation processing using a coarse-to-fine cross-correlation scheme coupled with iterative image deformation. A final sample size of 48 × 48 pixels resulted in vector validation rates exceeding 99% when applying a normalized median outlier detection scheme (Westerweel & Scarano, 2005).

With sequence lengths of 10 s the data sets consist of up to 25 000 velocity maps at a corresponding frequency of 2500 Hz (400 µs time interval). Fig. 6 provides first and second order statistics of the wake flow and is compiled from three different sampled areas of the cylinder wake. Discontinuities between the individual areas are due to small misalignments and minor unsteadiness of the channel's bulk flow.

Both proper orthogonal decomposition (POD) its extension to the frequency domain, spectral proper orthogonal decomposition (SPOD, Schmidt & Colonius, 2020) were applied to the recovered velocity data sets to further illustrate the potential of EBIV as a tool for fluid dynamics studies. Fig. 7 shows the relative contribution of the individual modes for both of the velocity components, u, v, as well as the estimated out-of-plane vorticity, ω_z, and in-plane divergence $\nabla_{xy} = (\partial u/\partial x + \partial v/\partial y)$. Due the higher noise level of the differential quantities, their energy is distributed across a higher number of modes. Reconstructed modes of the four quantities are provided in Fig. 8 with the contour level ranges scaled according to the modes' relative energy contributions.

From a fluid mechanical point of view, significant POD modes of the divergence ∇_{xy} appear downstream of $x/D > 3$. Given the incompressibility of the flow, $\nabla_{xy} = -\partial w/\partial z$ indicates that the wake flow is essentially 2-d up to $x/D \approx 3$ and becomes 3-d thereafter. This could also be observed in animations of the raw event data. The position also coincides with the location at which large vortical structures that are initially formed in the shear layers on either side of the cylinder's recirculation zone are alternatingly shed into the wake. This is also reflected by high POD amplitudes of the transverse velocity component at this position. It should be mentioned that the small aspect ratio

of cylinder diameter to channel width of $d/H = 1/7.6$ not only introduces blockage effects but also prevents the formation of a classical vortex street and instead results in a highly three-dimensional flow.

SPOD was performed on the data using the pySPOD package (Mengaldo & Maulik, 2021). Representative eigenspectra are provided in Fig. 9, corresponding first and second order modes in Fig. 11. The frequency spectra for both velocity components show a distinct peak at about 20 Hz that corresponds to the dominant shedding frequency in the cylinder wake. An energy decay rate typical for turbulent flows is present up to a frequency of about 100 Hz beyond which the slope of the spectra reduces. This can be attributed to noise in velocity estimates and is commonly present in spectra obtained from PIV data. Considerable energy is located at the low-frequency end peaking near 1 Hz and is barely resolved by the Fourier transform ($N_{\mathrm{FFT}} = 2048$, binwidth 1.2 Hz). This is believed to be caused by low-frequency modulation of the channel's bulk flow as it was being operated well outside of its typical velocity range. A broadband peak in the frequency range of 200–600 Hz is related to the operation of the detector itself (row-wise time-stamping of events). This peak becomes increasingly pronounced as the arbiter (read-out unit of the sensor) begins to saturate with pending events that are handled with increasing delay. An example of this is given in Fig. 10.

4. Conclusions

The previous example of EBIV applied to a cylinder wake flow intends to demonstrate its possible use as fluid flow measurement tool. It is clear, that both on the hardware as well as on the algorithmic side, there is considerable room for improvement. The fact that the previously described EBIV merely involves a camera (current cost 1500–3000 Euro) and a reasonably priced CW laser or LED (1–5 W range) is appealing, especially in the educational context (e.g. student labs).

The concepts of event-based imaging along with the associated imaging hardware are still quite young and continuously undergoing development. At the present maturity level of the event cameras the application of EBIV in air flows is a challenging one as the user needs to carefully match a number of interrelated parameters to obtain optimal results. On the one hand the particle image velocity on the sensor (e.g. pixel/s) should be kept within in range that reliably triggers events. With the present hardware this limits velocity measurements to about 1 m/s on a FOV of 50 mm. To a certain degree a reduction of the magnification allows the velocity range to be linearly increased but this requires a proportional increase of the illumination power or the use of larger particles, such as hydrogen filled soap bubbles (HFSB, Borer et al., 2017; Rusch & Rösgen, 2021; Rusch & Rösgen, 2022). The application of EBIV in water flows, such as reported by Willert & Klinner (2022), was found to be considerably less difficult, mainly due to the generally lower flow speeds and the possibility of using larger particles with a higher scattering efficiency.

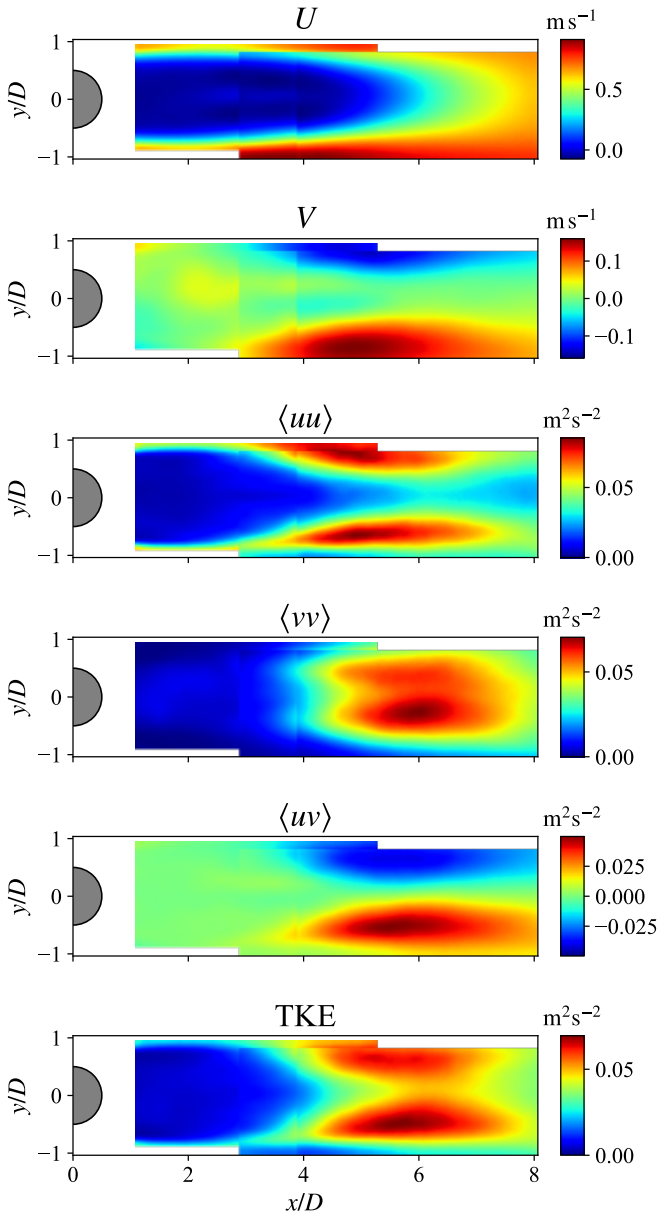

Figure 6. First order, second order statistics and turbulent kinetic energy of a cylinder wake flow at $\mathrm{Re}_D \approx 530$ assembled from three event recording sequences of up to 10 s duration.

References

Borer, D., Delbruck, T., & Rösgen, T. (2017). Three-dimensional particle tracking velocimetry using dynamic vision sensors. *Experiments in Fluids*, *58*(165). DOI: 10.1007/s00348-017-2452-5

Finateu, T., Niwa, A., Matolin, D., Tsuchimoto, K., Mascheroni, A., Reynaud, E., … Posch, C. (2020). 5.10 - A 1280×720 back-illuminated stacked temporal contrast event-based vision sensor with 4.86 µm pixels, 1.066GEPS readout, programmable event-rate controller and compressive data-formatting pipeline. In *2020 IEEE International Solid- State Circuits Conference - (ISSCC)* (p. 112-114). DOI: 10.1109/ISSCC19947.2020.9063149

Gallego, G., Delbrück, T., Orchard, G., Bartolozzi, C., Taba, B., Censi, A., … Scaramuzza, D. (2022).

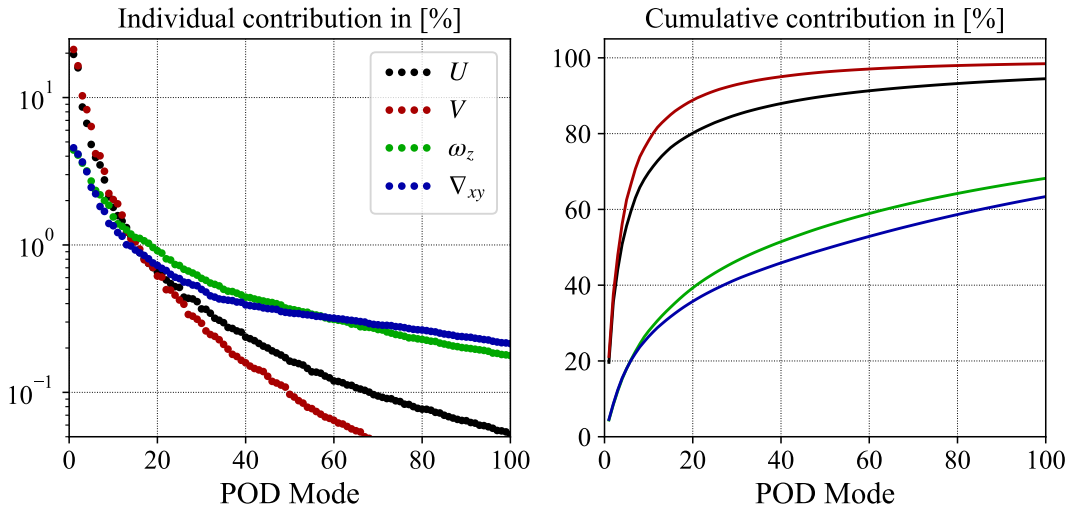

Figure 7. Relative and cumulative contribution of the POD modes in the cylinder wake flow at $\mathrm{Re}_D \approx 530$.

Event-based vision: A survey. *IEEE Transactions on Pattern Analysis and Machine Intelligence*, *44*(1), 154-180. DOI: 10.1109/TPAMI.2020.3008413

Lichtsteiner, P., Posch, C., & Delbruck, T. (2008). A 128×128 120 dB 15 µs latency asynchronous temporal contrast vision sensor. *IEEE Journal of Solid-State Circuits*, *43*(2), 566-576. DOI: 10.1109/JSSC.2007.914337

Mahowald, M. (1992). *VLSI analogs of neuronal visual processing: a synthesis of form and function* (Doctoral dissertation, California Institute of Technology, Pasadena (CA)). Retrieved from `https://resolver.caltech.edu/CaltechCSTR:1992.cs-tr-92-15`

Mengaldo, G., & Maulik, R. (2021). PySPOD: A Python package for spectral proper orthogonal decomposition (SPOD). *Journal of Open Source Software*, *6*(60), 2862. DOI: 10.21105/joss.02862

Robotics and Perception Group. (2022). *Event-based vision resources.* `https://github.com/uzh-rpg/event-based_vision_resources`. GitHub. Retrieved from `https://github.com/uzh-rpg/event-based_vision_resources`

Rusch, A., & Rösgen, T. (2021, Sep). TrackAER: Real-time event-based particle tracking. In *14th international symposium on particle image velocimetry (ispiv 2021)* (p. 176). Chicago, IL: Illinois Institute of Technology. DOI: 10.18409/ispiv.v1i1.176

Rusch, A., & Rösgen, T. (2022, July). Online event-based insights into unsteady flows with TrackAER. In *20th international symposium on application of laser and imaging techniques to fluid mechanics.* Lisbon, Portugal.

Schmidt, O. T., & Colonius, T. (2020). Guide to spectral proper orthogonal decomposition. *AIAA Journal*, *58*(3), 1023–1033. DOI: 10.2514/1.J058809

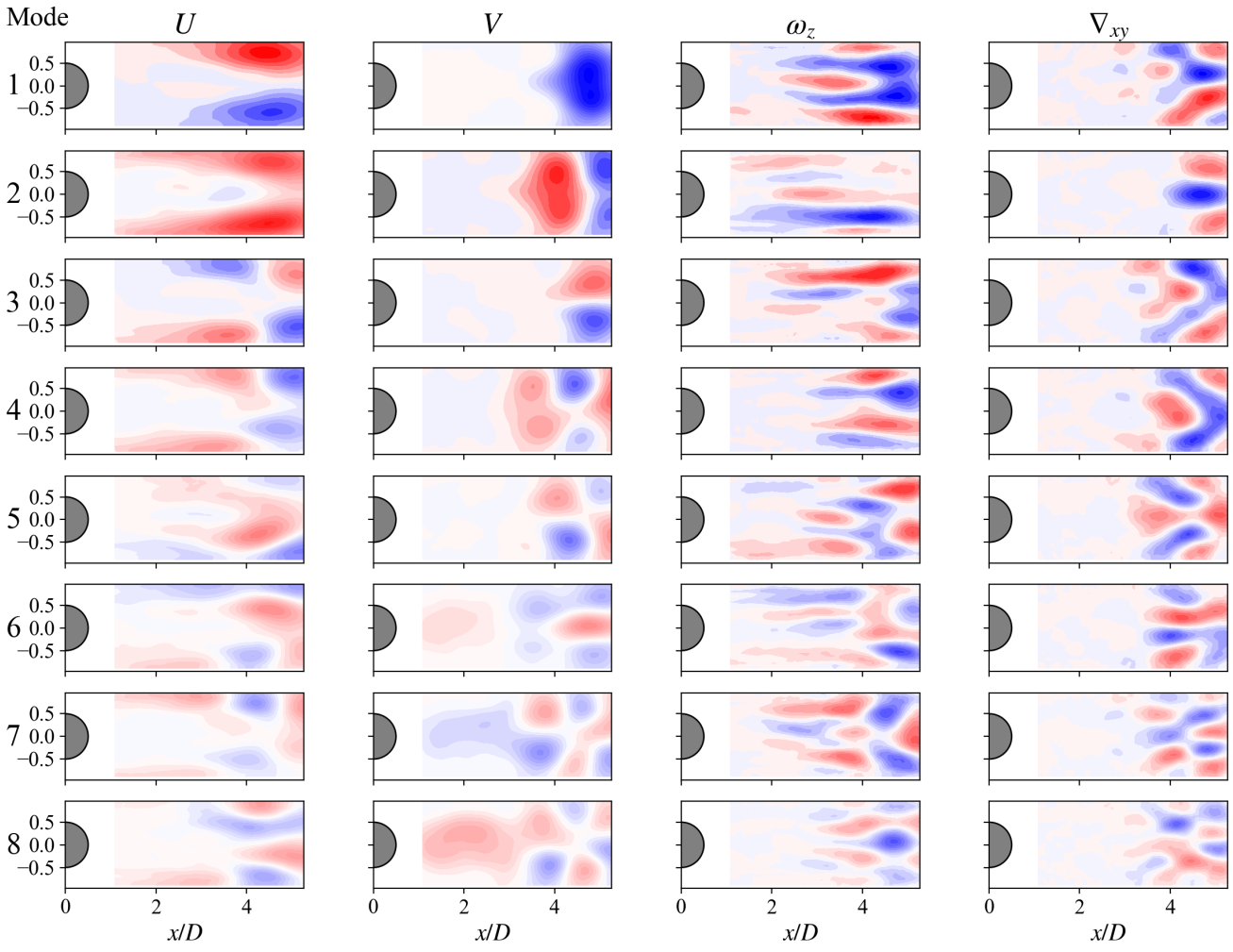

Figure 8. First 8 POD modes in the cylinder wake flow at $\mathrm{Re}_D \approx 530$. Intensity values of the modes are scaled according to the mode's relative energy contribution.

Tayarani-Najaran, M.-H., & Schmuker, M. (2021). Event-based sensing and signal processing in the visual, auditory, and olfactory domain: A review. *Frontiers in Neural Circuits*, *15*. DOI: 10.3389/fncir.2021.610446

Westerweel, J., & Scarano, F. (2005). Universal outlier detection for piv data. *Experiments in Fluids*, *39*(6), 1096-1100. DOI: 10.1007/s00348-005-0016-6

Willert, C., & Klinner, J. (2022). Event-based imaging velocimetry: An assessment of event-based cameras for the measurement of fluid flows. *Exp. Fluids*. DOI: 10.1007/s00348-022-03441-6

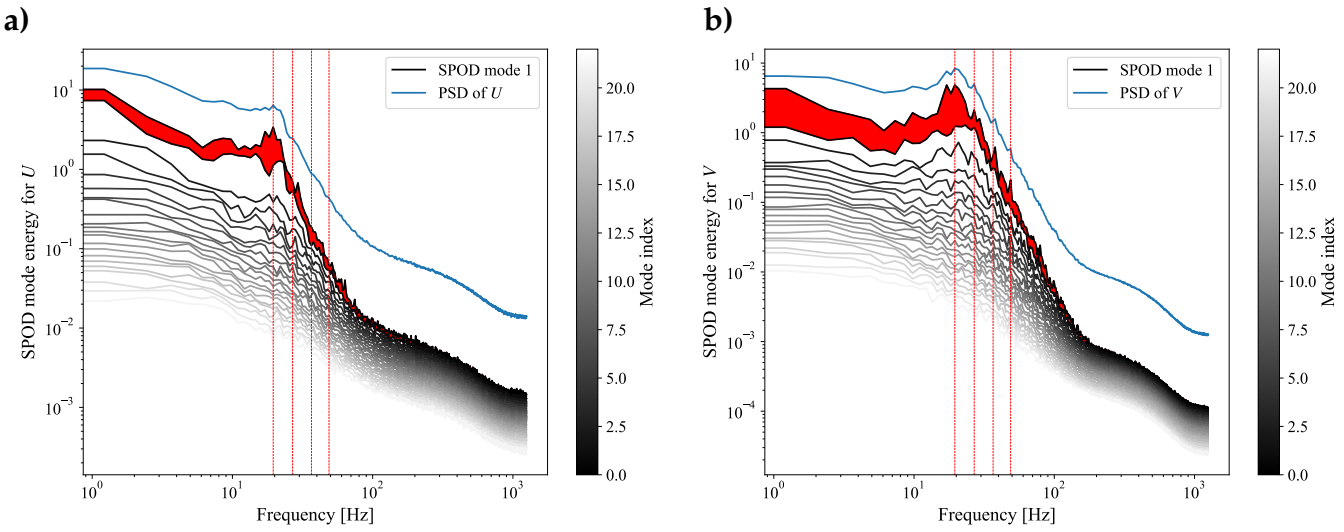

Figure 9. Spectra of the cylinder wake obtained with SPOD, for the streamwise velocity component (**a**) and transverse component (**b**). The power spectral density (PSD) is represents the average PSD over all grid points.

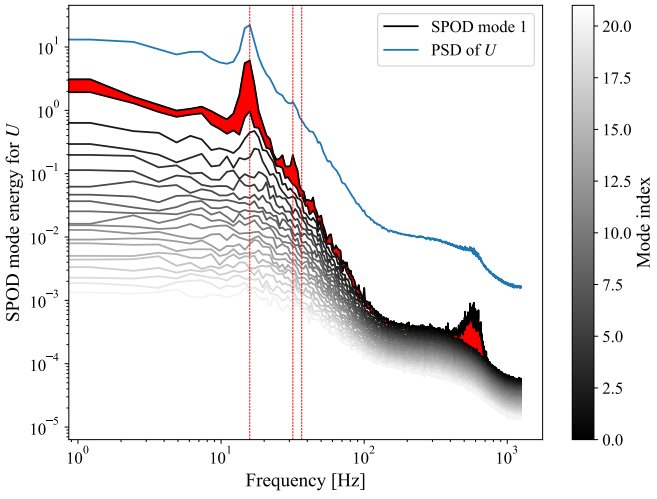

Figure 10. SPOD spectra of the cylinder wake flow obtained from event data contaminated with noise due partial event overflow on the event sensor.

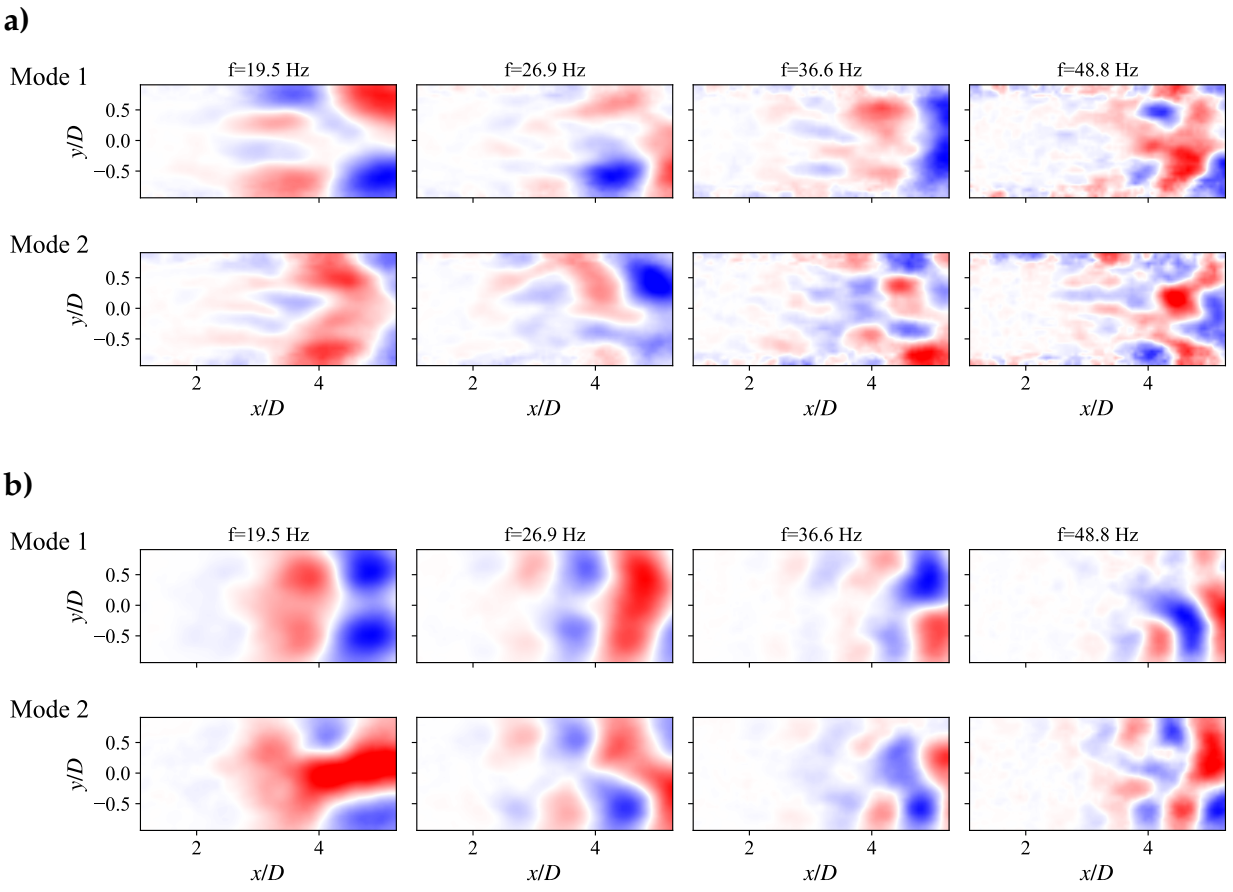

Figure 11. First order SPOD modes of the cylinder wake at representative frequencies shown in Fig. 9 for the streamwise velocity component (**a**) and transverse component (**b**).